

18 Abstract

19 In this study, we employ the Grid Agnostic Magnetohydrodynamic (MHD) for Extended Research
20 Applications (GAMERA), a high-resolving power, three-dimensional global MHD model, to
21 simulate magnetotail reconnection in Jupiter's magnetosphere. While previous satellite
22 observations have provided initial statistics on magnetotail reconnection properties at Jupiter, they
23 have been limited in space-time coverage, leaving the dynamic process of Jovian magnetotail
24 reconnection and its response to the solar wind (SW) poorly understood. Using MHD simulations,
25 we quantitatively analyze the temporal evolution and spatial dependence of nightside reconnection
26 in Jupiter's magnetotail under ideal quiet and enhanced SW conditions. Our results demonstrate
27 that magnetotail reconnection tends to occur in the midnight and post-midnight sectors, with a low
28 occurrence in the pre-midnight sector, consistent with both Galileo and Juno observations and
29 predictions by Delamere and Bagenal (2013). The MLT-radial distribution of magnetotail
30 reconnection is broad, indicating that Jovian magnetotail reconnection is always dynamic rather
31 than steady-state. Enhanced SW ram pressure can decrease the MLT coverage of magnetotail
32 reconnection by compressing Jupiter's magnetosphere. However, the occurrence of magnetotail
33 reconnection near the midnight and post-midnight sectors is enhanced by SW compression beyond
34 ~ 60 RJ, but is not significantly impacted by SW compression within ~ 60 RJ. Conversely, SW
35 compression suppresses reconnection in the pre-midnight sector, leading to a stronger dawn-dusk
36 asymmetry in the occurrence and location of magnetotail reconnection. This study validates the
37 applicability of the GAMERA code for simulating Jupiter's magnetosphere and provides
38 complementary insights into the dynamic structure and the SW response of Jupiter's
39 magnetosphere.

40 Plain Language Summary

41 Magnetic reconnection is a fundamental plasma process that plays a crucial role in rearranging
42 magnetic fields and converting energy in the planetary magnetosphere. Understanding this process
43 is pivotal in comprehending the structure and dynamics of planetary magnetospheres, particularly
44 in the magnetotail region. In contrast to Earth, where the dynamics in the magnetotail range are
45 primarily driven by the merging of solar winds, Jupiter's magnetotail dynamics are mostly
46 dominated by planetary rotation due to its large magnetospheric size, strong magnetic field strength,
47 and fast rotation speed. Thus, Jupiter's magnetotail is unique and provides valuable insights into

48 the interplay between magnetic reconnection and planetary magnetospheres. Although spacecraft
49 have made direct observations of reconnection events, the dynamic structure of magnetotail
50 reconnection and its response to the solar wind compression are still not well understood. To gain
51 a better understanding, this study uses a global MHD code and specifically focuses on the temporal
52 evolution and spatial variation of Jovian magnetotail reconnection and its dependence on the solar
53 wind ram pressure.

54 **1 Introduction**

55 Magnetic reconnection is a fundamental process in laboratory and space plasma systems, involving
56 the rearrangement of magnetic topology and energy conversion (Parker, 1979; Biskamp, 1996;
57 Priest & Forbes, 2000; Yamada et al., 2010). This process plays a crucial role in shaping the
58 structure and dynamics of planetary magnetospheres, particularly in the magnetotail region where
59 the magnetic field lines are stretched out by the solar wind (SW). Among all the known
60 magnetotails in the solar system, Jupiter's magnetotail stands out as a unique laboratory for
61 studying space plasma physics due to its unparalleled characteristics such as the largest size, the
62 strongest magnetic field strength, and the fastest rotation.

63 In contrast to Earth, where the magnetospheric dynamics are primarily determined by magnetic
64 reconnection between the SW/interplanetary magnetic field (IMF) and planetary magnetic field,
65 the dynamics in the Jovian magnetosphere, including its magnetotail region, are mostly driven by
66 planetary rotation due to the large Jovian corotation potential (e.g., Khurana et al., 2004; McComas
67 & Bagenal, 2007, 2008) and also affected by the viscous-like solar wind interaction (Delamere &
68 Bagenal, 2010; Masters, 2018). Although there is some debate about the importance of SW
69 reconnection in the Jovian magnetosphere (Cowley et al., 2003; Cowley et al., 2008). The unique
70 dynamics of Jovian magnetotail reconnection can exacerbate the loss of the internal plasma,
71 particularly from the Io torus, to the far magnetotail (Kurth et al., 1982; Khurana et al., 2004;
72 Thomas et al., 2004), and may induce distinctive aurora morphology (e.g., Waite et al., 1994; Ajello
73 et al., 1998; Waite et al., 2001; Mauk et al., 2002; Szego et al., 2016; Connerney et al., 2017;
74 Gladstone et al., 2017; Gérard et al., 2018; Grodent et al., 2018; Bonfond et al., 2020; Yao et al.,
75 2020; Guo et al., 2021; Yao et al., 2022). Hence, investigating the Jovian magnetotail reconnection
76 provides valuable insights into the complex interplay between magnetic reconnection and the

77 dynamics of planetary magnetospheres, with important implications for our understanding of space
78 weather and auroral processes in the Jovian magnetosphere.

79 The Vasyliunas cycle is a well-established theoretical model for describing the average state of
80 magnetotail reconnection and plasma circulation at Jupiter (Vasyliunas, 1983). In the Jovian
81 nightside magnetotail, the centrifugal force exerted by the co-rotating plasma can elongate the
82 internal quasi-dipole magnetic flux tubes. As a result, the antiparallel directions or components of
83 the stretched magnetic field lines may reconnect near the equatorial plane, resulting in plasmoid
84 ejections down the magnetotail. Based on this theory and an array of observations and simulations,
85 Delamere and Bagenal (2013) put forth an enhanced theoretical prediction for the Vasyliunas cycle.
86 This prediction takes into account the size of the magnetosphere, which is related to strong viscous-
87 like interaction and the momentum transfer rate from the solar wind, and incorporates locations of
88 various structures, including the tail reconnection X-line.

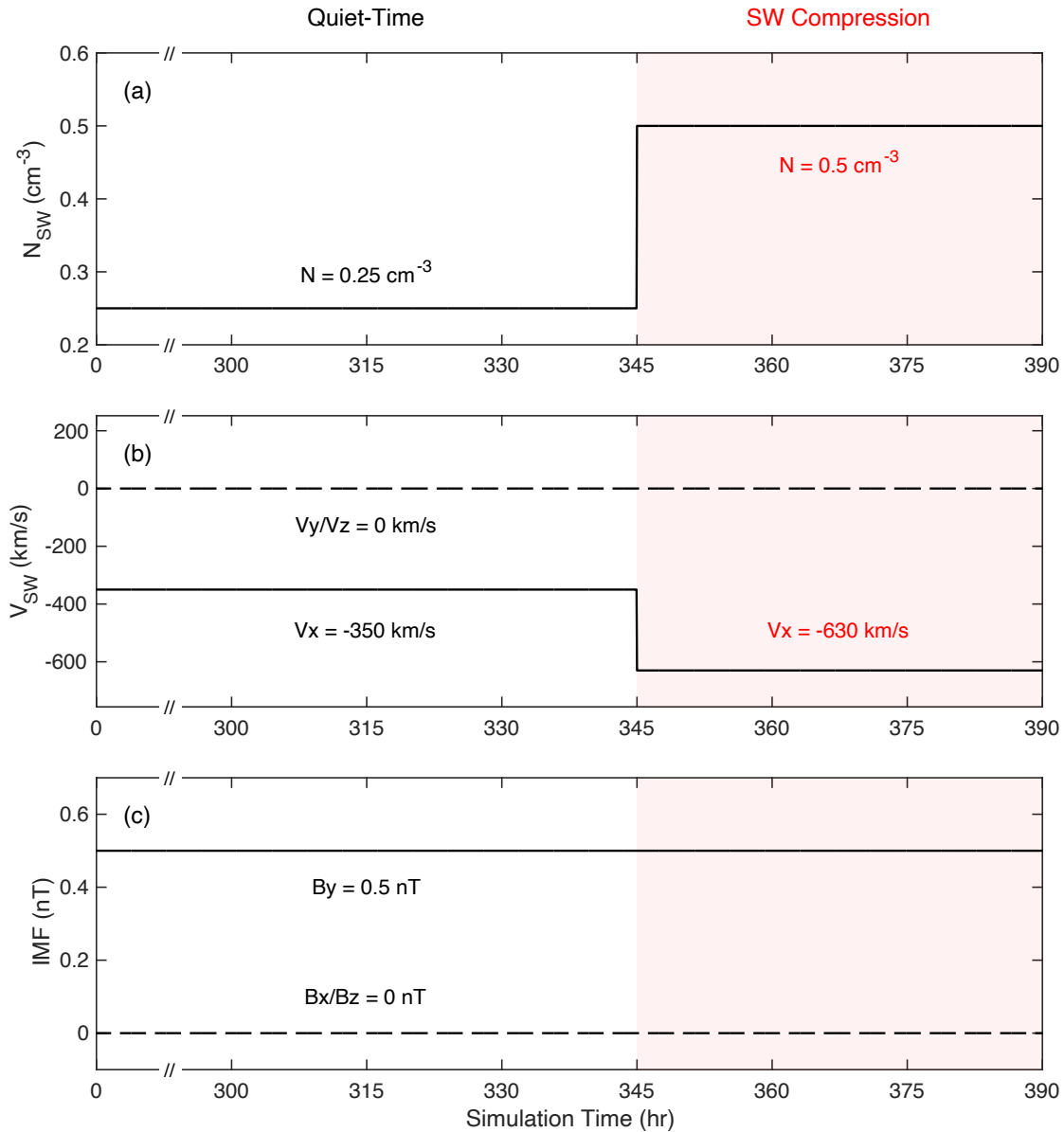
89 Direct observations of reconnection events in the Jovian magnetotail have been made by the
90 Voyager 1 and 2 flybys in 1979 (Nishida, 1983), the Galileo spacecraft from late 1995 to 2003
91 (e.g., Russell et al., 1998; Woch et al., 2002; Kronberg et al., 2005; Vogt et al., 2010) and the Juno
92 spacecraft from July 2016 to present (Vogt et al., 2020), providing important statistics of
93 reconnection event properties such as their spatial extent, recurrence time, and location. Plasma
94 measurements in Jupiter's magnetotail for $\sim 2000 R_J$ downstream were also provided by the recent
95 flyby of Jupiter by the New Horizons spacecraft (McComas & Bagenal, 2007; McNutt et al., 2007),
96 although without magnetometer data, the periodicities in the energetic particle dispersive events
97 suggest plasmoid release from magnetotail reconnection (M. E. Hill et al., 2009). However, due to
98 insufficient data coverage of observations and the inseparability of space-time information in
99 single-spacecraft measurements, the dynamic structure of magnetotail reconnection and its
100 response to the SW have not been well understood. In addition, previous studies using
101 magnetohydrodynamic (MHD) codes have simulated the magnetotail structures at Jupiter (e.g.,
102 Ogino et al., 1998; Miyoshi & Kusano, 2001; Song et al., 2001; Moriguchi et al., 2008; Chané et
103 al., 2013; Wang et al., 2018; Sarkango et al., 2019; Tanaka et al., 2021), but lacked quantitative
104 comparison of magnetotail reconnection with Galileo/Juno Observations and the prediction by
105 Delamere and Bagenal (2013).

106 The recent development of the Grid Agnostic MHD for Extended Research Applications
107 (GAMERA), a high-resolving power, three-dimensional global MHD code (Lyon et al., 2004;
108 Zhang et al., 2019), has enabled the study of SW-Jupiter interactions with mesoscale-resolving
109 capabilities (Zhang et al., 2018; Zhang et al., 2021; Feng et al., 2022, Chen et al., 2023). In this
110 study, we use the GAMERA code to simulate the dynamic structure of Jupiter’s magnetotail and
111 its response to the SW ram pressure. First, we show the effectiveness of the MHD model on the
112 Jovian magnetospheric problems by comparing the simulated radial density profile within Jupiter’s
113 magnetodisc with observations. Then, we quantitatively analyze the temporal evolution and spatial
114 dependence of nightside reconnection in Jupiter’s magnetotail. Furthermore, the response of the
115 Jovian magnetotail reconnection to SW compression is investigated by comparing the magnetotail
116 structures under ideal quiet and enhanced SW conditions.

117 **2 Methods**

118 **2.1 The global MHD model**

119 For simulating the space environment of Jupiter’s magnetosphere, the GAMERA code uses a
120 finite-volume technique to solve the ideal MHD equations on a non-orthogonal, curvilinear grid
121 that is adapted to the Jovian magnetospheric problems. The computational grids are based on non-
122 orthogonal stretched spherical grids with $256 \times 256 \times 128$ cells corresponding approximately to the
123 spherical (radial \times meridional \times azimuthal) coordinate. The grids are oriented in solar-
124 magnetospheric coordinates, where the X, Y, and Z axes correspond to the Sun, east (dusk), and
125 north, respectively. The grid resolution varies with radial distance to the planetary center, with the
126 highest radial resolution of ~ 0.14 Jovian Radii (R_J) near the inner boundary, which is located at a
127 Jovi-centric distance of $3 R_J$. The Jovian magnetospheric simulation extends to $100 R_J$ in the
128 sunward direction, $-1000 R_J$ in the anti-sunward direction, and $\pm 300 R_J$ in directions perpendicular
129 to the Sun-Jupiter axis. To simplify the analysis by removing hemispheric asymmetries induced
130 by the tilt, the dipole tilt angle of the Jovian magnetosphere is set to 0. The 10-hour corotation of
131 the Jovian magnetosphere is implemented by imposing a time-stationary corotation potential onto
132 the ionospheric potential (Zhang et al., 2018). The simulated heavy-ion massing loading from the
133 Io plasma torus is 1000 kg/s , added in a ring centered at $6 R_J$ in the equatorial plane. The output
134 time step is 600 s .



135

136 **Figure 1.** The upstream solar wind (SW)/ interplanetary magnetic field (IMF) conditions as used in the simulation.

137

Shown from top to bottom are (a) SW density, (b) SW velocity, and (c) IMF.

138

139

140

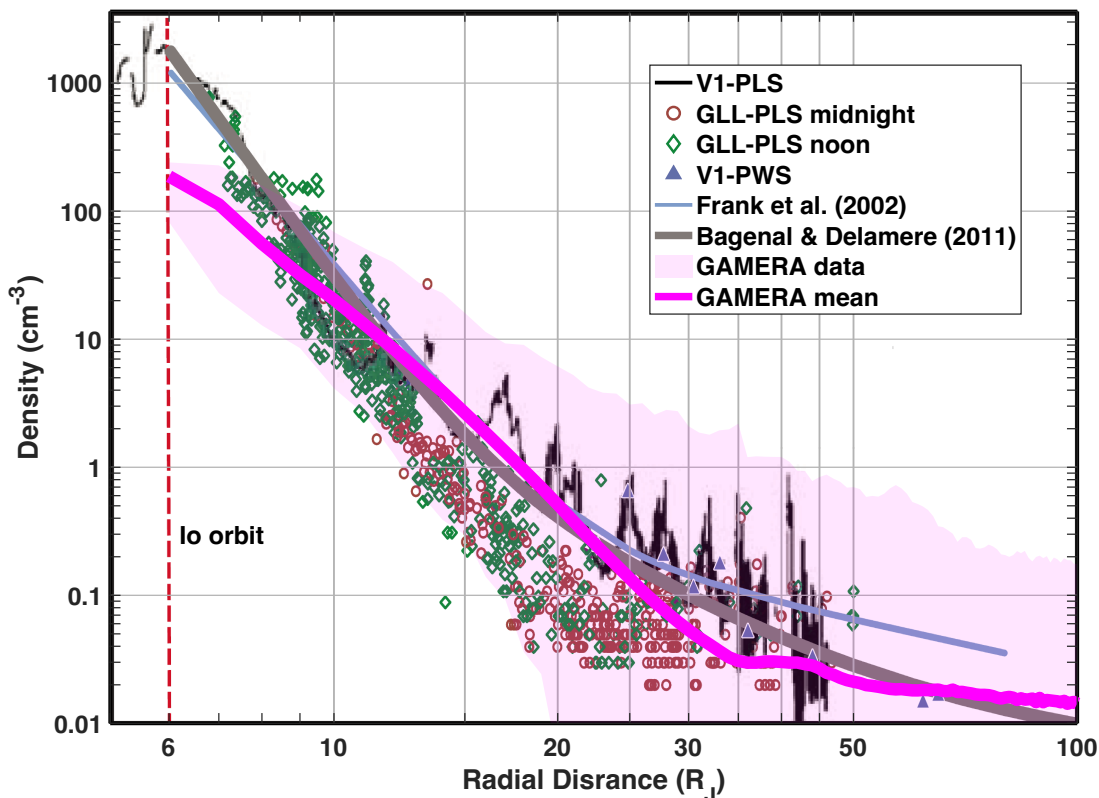
141

142

143

Figure 1 depicts the upstream SW/ IMF conditions that drive the global MHD model of Jupiter's magnetosphere. During the initial 0–345 hrs simulation time (ST), the upstream SW temperature, density, velocity, and IMF B_y are set to quiet-time parameters of 2.0×10^4 K, 0.25 cm⁻³, 350 km/s, and 0.5 nT, respectively, corresponding to Alfvén Mach numbers of 16.0, based on typical SW/IMF conditions (Blanc et al., 2005; Delamere & Bagenal, 2010; Jackman & Arridge, 2011). It should be noted that this study analyzes only the simulation data after the start-up transit (~ 300 hr) when

144 the average radial profile of the heavy ion density was settled into a quasi-steady state in a spin-
 145 averaged sense. To analyze the response of magnetotail reconnection after an SW compression,
 146 SW density and velocity are set to enhanced parameters of 0.5 cm^{-3} and 630 km/s during 345:00–
 147 390:00 ST, corresponding to Alfvén Mach numbers of 40.8. For convenience, 300:00–345:00 ST
 148 is referred the quiet-time period, and 345:00–390:00 ST is called the SW compression period.



149
 150 **Figure 2.** Radial density profile in the simulation, compared with Figure 1 from Bagenal and Delamere (2011). The
 151 magenta shadow represents the simulated equatorial density data averaged over 300:00–390:00 ST, while the magenta
 152 line represents the azimuthal-mean density. Density measurements derived from Voyager 1 PLS (black line), Voyager
 153 1 PWS (blue triangles), and Galileo PLS (all orbits) obtained $\pm 30^\circ$ around noon (green diamonds) and $\pm 30^\circ$ around
 154 midnight (red circles). The profile from Frank et al. (2002) (pale blue curve) is based on Galileo PLS data from the
 155 G8 orbit data obtained on the nightside. The profile from Bagenal and Delamere (2011) (thick gray curve) is a
 156 composite of three power law profiles (blue, purple, and yellow lines).

157 Figure 2 compares the radial density profile within Jupiter’s magnetodisc in the MHD simulation
 158 with observations to evaluate the effectiveness of the simulation in addressing Jovian
 159 magnetospheric issues. Within the range of 10–100 R_J , which encompasses the majority of
 160 observed Jovian magnetotail reconnection events in the range of 37.5–124.2 R_J (Vogt et al., 2010;

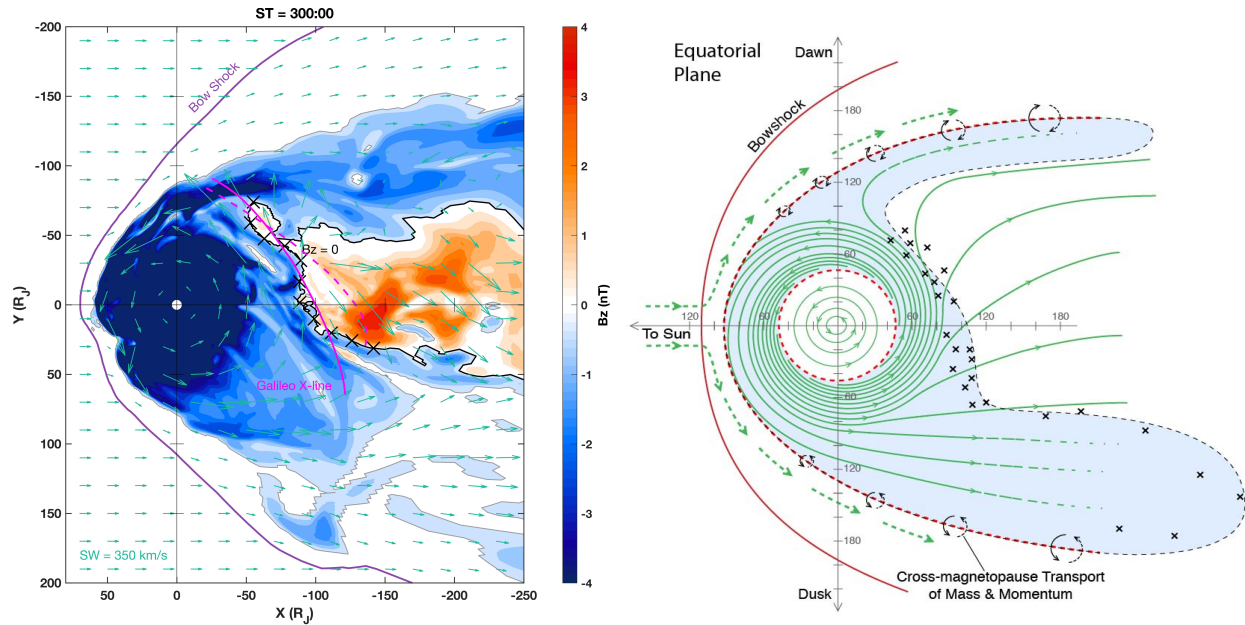
161 Vogt et al., 2020), our simulated density profiles exhibit an excellent agreement with in situ
162 measurements and empirical distributions summarized by Bagenal and Delamere (2011).
163 Furthermore, the simulated density displays significant relative variations, as shown in the
164 magenta shadow in Figure 2. Schok et al. (2023) found the relative density variations in the
165 GAMERA simulation between 10–60 R_J were in agreement with the Juno observations between
166 30–50 R_J (Huscher et al., 2021). These observation-simulation agreements validate that the MHD
167 model is a suitable tool for investigating the dynamic evolution of the Jovian magnetosphere,
168 including the magnetotail reconnection process.

169 Note that magnetic reconnection in the MHD simulation is enabled by numerical resistivity, i.e.,
170 when opposing magnetic flux enters a single computational cell and is then averaged out of
171 existence (Brambles et al., 2011). The rate of reconnection is determined only by the conditions
172 external to the actual reconnection region through the conservation of mass, momentum, and
173 magnetic flux (Lyon et al., 2004; Zhang et al., 2016; Zhang et al., 2017). In the simulation of the
174 terrestrial magnetosphere, Ouellette et al. (2013) have shown that when reconnection is induced
175 by convergent flow, the nightside reconnection rate in the simulation is constrained by a Petschek-
176 like inflow condition to be a fraction (≈ 0.1) of the Alfvén speed in the inflow, regardless of the
177 grid size. Thus we expect that the global MHD simulation is capable of reproducing large-scale
178 configuration of Jovian magnetotail reconnection, although micro-physics has not been
179 implemented into the Jovian magnetosphere simulation.

180 **2.2 Locating the B_z reversal positions**

181 In a planetary magnetosphere without dipole tilt and significant hemispheric asymmetry,
182 magnetotail reconnection at the equatorial plane can be identified in the magnetic field by tracking
183 changes in the north-south component of the magnetic field (B_z), such as field dipolarizations or
184 B_z reversals (Vogt et al., 2010). In this study, we used a similar method as suggested by Vogt et al.
185 (2010) to find the positions of magnetotail reconnection, but applied it to the high-resolution
186 simulation data. Specifically, we sliced the data at the equatorial plane ($Z = 0$) at evenly 600-
187 second spaced steps during 300:00–390:00 ST and identified positions where B_z reversed from
188 southward (parallel to the background field) to northward (antiparallel) as radial distance increases
189 for each azimuthal index on the nightside ($X < 0$). Figure S1 provides an example of B_z reversal
190 positions at 300:00 ST. It is important to note that the identified B_z reversal positions may not

191 necessarily correspond to the actual locations where reconnection first occurs when there are radial
 192 outflow transports in the magnetotail (Movie S1); however, this method allows for a useful
 193 comparison between simulations and observations.



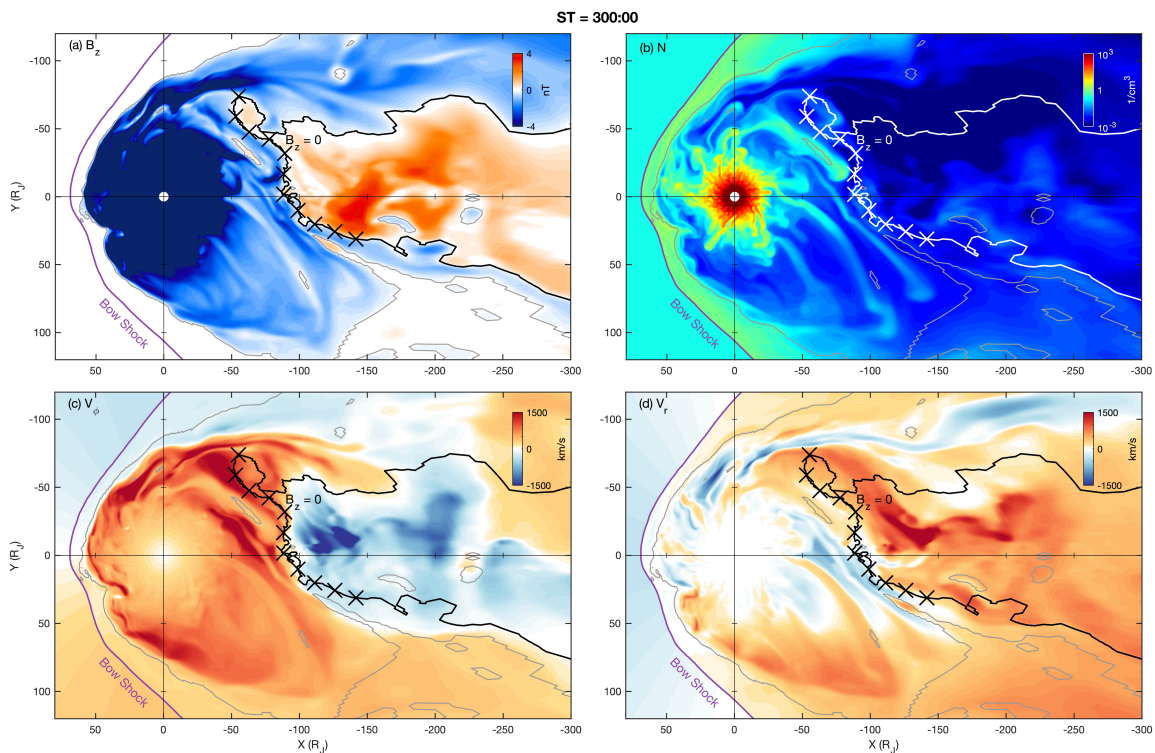
194
 195 **Figure 3.** (left) The simulated distribution of B_z (positive northward) and plasma flow at the equatorial plane of
 196 Jupiter's magnetosphere at 300:00 ST. Black/gray lines indicate the B_z zero lines, "X" patterns mark approximate
 197 locations of the X-line, and green arrows represent plasma flows. Additionally, a magenta solid line represents the
 198 average location of the X-line based on Galileo magnetic field data from Vogt et al. (2010), and a magenta dashed
 199 line denotes the average location of the X-line based on Galileo particle flow data from Woch et al. (2002), excluding
 200 the premidnight results with large uncertainty. (right) A schematic of theoretical prediction of the equatorial meridians
 201 for the Vasyliunas cycle, adapted from Delamere and Bagenal (2013), showing the average plasma flow (green), the
 202 predicted locations of the X-line ("X" pattern), and the regions of closed magnetic flux (light blue). The wings of
 203 closed flux on the dawn and dusk flanks are taken from global MHD simulations (Song et al., 2001; Jia et al., 2012)
 204 and based on New Horizons dispersive events (McNutt et al., 2007; M. E. Hill et al., 2009).

205 3 Results

206 3.1 Global configuration of Jovian magnetotail reconnection

207 Figure 3 depicts (left) an instantaneous distribution of the simulated B_z and plasma flow in the
 208 equatorial plane of the Jovian magnetosphere, compared with the Galileo-observed X-lines based
 209 on B_z (magenta solid lines) and plasma flow data (magenta dashed line) and (right) a theoretical
 210 prediction for the Vasyliunas cycle in Delamere and Bagenal (2013). Besides B_z reversals,
 211 magnetotail reconnection may also be identified by the reversals of the disturbances in the radial

212 and azimuthal components of the particle flow (Woch et al., 2002). As shown in the left panel of
213 Figure 3, the two Galileo-observed X-lines from B_z (magenta solid line) and plasma flow data
214 (magenta) generally correspond with each other. In the following we mainly compare the MHD
215 results with the Galileo B_z X-line. Within approximately Jovi-centric 100 R_J of the simulated
216 Jovian magnetotail near the midnight meridian, where B_z is parallel with the southward component
217 of internal planetary dipole fields, and magnetospheric plasma corotates in the counterclockwise
218 direction when viewed above the North Pole. Near the midnight meridian outside Jovi-centric 100
219 R_J , B_z has significant south-to-north reversals with the order of 1–4 nT in a cavity (red ranges
220 enclosed by the black line), where plasma flows are generally radially outward and have clockwise
221 azimuthal components. The coverage of the B_z -reversed cavity shows a dawn-dusk asymmetry
222 that is wider on the dawnside than on the duskside. Beyond the B_z -reversed cavity, there are wing
223 structures of southward B_z on the dawn flank and of disturbed B_z on the dusk flank. The simulated
224 large-scale structure of corotation ranges, B_z -reversed cavity and B_z -southward/disturbed wings in
225 Jupiter’s internal magnetotail is generally consistent with the theoretical picture (the right panel of
226 Figure 3). Specifically, the “X” patterns in the left panel of Figure 3 represent approximate
227 locations of magnetotail reconnection in the simulation, which are located at the “inner” side of
228 the magnetotail B_z -zero line. The simulated X-line has a radial distribution similar to those
229 predicted by Delamere and Bagenal (2013) (“X” patterns in the right panel) and observed by the
230 Galileo satellite (magenta line in the left panel). However, the MHD simulation and the theoretical
231 prediction in Figure 3 differ in terms of the magnetospheric size and duskside wings. This
232 difference is a consequence of the fact that the MHD result shown in Figure 3 is just an
233 instantaneous snapshot of the highly dynamic Jovian magnetosphere under ideal SW conditions as
234 shown in Movie S1, whereas the theoretical prediction is based on an average of the statistical data
235 with changing real SW conditions.



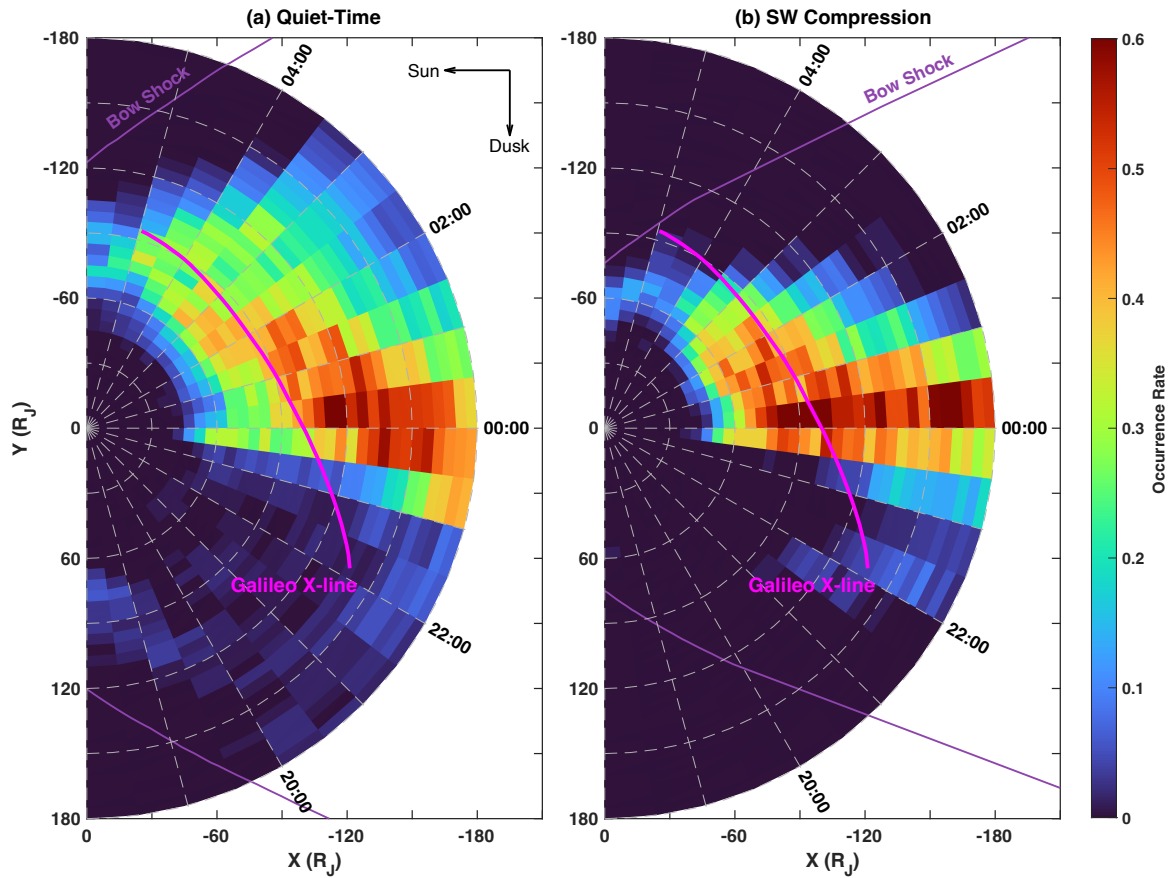
236
 237 **Figure 4.** The distribution of (a) B_z (positive northward), (b) plasma number density (N), (c) azimuthal flow (V_ϕ ,
 238 positive anticlockwise), and (d) radial flow (V_r , positive outflow) at the equatorial plane of Jupiter’s magnetosphere
 239 at 300:00 ST from the MHD simulation. The same snapshot is shown in Figure 3a. The contours of $B_z = 0$ are
 240 represented by black/white and gray lines in each panel, “X” patterns denote the approximate locations of the X-line.
 241 To further understand the magnetotail reconnection process, Figure 4 presents distributions of B_z ,
 242 plasma number density, azimuthal and radial flow speeds derived from the same snapshot (300:00
 243 ST) as in the left panel of Figure 3. Figures 4a–4b show a dense disc-like structure of magnetic
 244 field and plasma density within Jovi-centric $30 R_J$, referred to as the magnetodisc (Delamere et al.,
 245 2015; Huscher et al., 2021). Notably, the magnetodisc displays periodic finger-like density-
 246 enhanced structures between Jovi-centric $6\text{--}40 R_J$ that corotate with Jupiter and extend outward
 247 (see the plasma velocity in Figures 4c–4d). These periodic structures are believed to be generated
 248 by the centrifugal force arising from planetary rotation, which was also seen in drift-kinetic
 249 simulations of the Jovian magnetosphere (Yang et al., 2019; Wang et al., 2023). Near the
 250 magnetotail reconnection locations (marked by “X” patterns), enhancements in clockwise/Jupiter-
 251 ward flows and in anticlockwise/tailward flows are evident (Figures 4c–4d). The consistency of
 252 the enhancements in radial and azimuthal flows is also observed in the observation (Woch et al.,

253 2002). These enhanced flow speeds are signatures of reconnection exhaust flows due to
254 magnetotail reconnection. The anticlockwise/outward flows generated by magnetotail
255 reconnection can transport the plasma mass and magnetic flux to distant magnetotail, which is
256 known as the plasmoid release process (Kronberg et al., 2005; Vogt et al., 2014). The dynamics of
257 this process are visualized in Movie S1.

258 **3.2 Statistical analysis of the magnetotail reconnection**

259 Movie S1 reveals that the magnetosphere of Jupiter exhibits three distinct phases over 300:00–
260 390:00 ST. The first phase occurs during the period of quiet-time SW between 300:00 and 345:00
261 ST, during which the magnetosphere extends to approximately 60–70 R_J on the dayside and
262 undergoes relatively stable but dynamic variations. The second phase occurs during the early
263 stages of SW compression between 345:00 and 360:00 ST, during which the magnetosphere is
264 rapidly compressed and the dayside scale is reduced from $\sim 60\text{--}70 R_J$ to $\sim 40\text{--}45 R_J$. This transient
265 phase is characterized by highly unstable energy and mass release processes in the magnetotail.
266 The third phase occurs during the later stages of SW compression between 360:00–390:00 ST, in
267 which the magnetosphere remains compressed to a relatively stable scale of 40–45 R_J on the
268 dayside. In this subsection, we focused primarily on the first and third phases, during which
269 Jupiter’s magnetosphere exhibited a relatively quasi-steady state rather than a transient state. The
270 second phase will be mentioned in the discussion.

271 The highly dynamic evolution of the Jovian magnetotail reconnection process exhibits a broad
272 radial-MLT coverage in the equatorial plane (Movie S1). To analyze the statistical distribution of
273 magnetotail reconnection, we performed a statistical analysis of the occurrence rate of B_z -reversal
274 cases following a similar method used in Figure 9 of Vogt et al. (2010). This statistical distribution
275 of the magnetotail reconnection is based on radial distance and MLT during quiet-time periods
276 (300:00–345:00 ST) and the later phase of SW compression periods (360:00–390:00 ST). Initially,
277 we segregated the equatorial B_z data from the MHD simulation into bins with a radial distance of
278 5 R_J and a 0.5-hr interval in MLT. Within each bin, if at least one grid showed a B_z reversal, we
279 identified that bin as a B_z reversal case and incremented the count by one. The occurrence rate was
280 computed as the number of steps with B_z reversal cases in each bin divided by the total steps
281 during the considered period, given that the output time step was 600 s.



282

283 **Figure 5.** The occurrence rate of B_z reversal cases in the MHD simulation for bins of $5 R_J$ in the radial distance and
 284 0.5 hr in MLT during (a) quiet-time periods between 300:00–345:00 ST, and (b) the later phase of SW compression
 285 between 360–390 ST. The occurrence rate is computed as the step counts with B_z reversal cases in each bin divided
 286 by the total steps, given that the output time step is 600 s. The count of B_z -reversal cases is incremented by 1 for each
 287 bin whenever at least one point in the bin exhibits B_z reversal. The magenta lines represent the average location of the
 288 X-line based on Galileo data, adapted from Vogt et al. (2010).

289 Figure 5 illustrates the spatial dependence in the occurrence of the B_z reversal cases during quiet-
 290 time periods and the later phase of SW compression periods. For both SW conditions, the simulated
 291 B_z reversal events are mostly outside Jovi-centric $35 R_J$, which is consistent with the fact that B_z
 292 reversal events were observed by Galileo between 44.09 – $124.2 R_J$ (Vogt et al., 2010) and Juno
 293 between 37.5 – $112.7 R_J$ (Vogt et al., 2020). Most B_z reversal cases occur near the midnight
 294 meridian around 0:00 MLT. The occurrence rate of B_z reversal cases in the post-midnight sector
 295 (0:00–6:00 MLT) is much higher than that in the pre-midnight sector (18:00–24:00 MLT). This

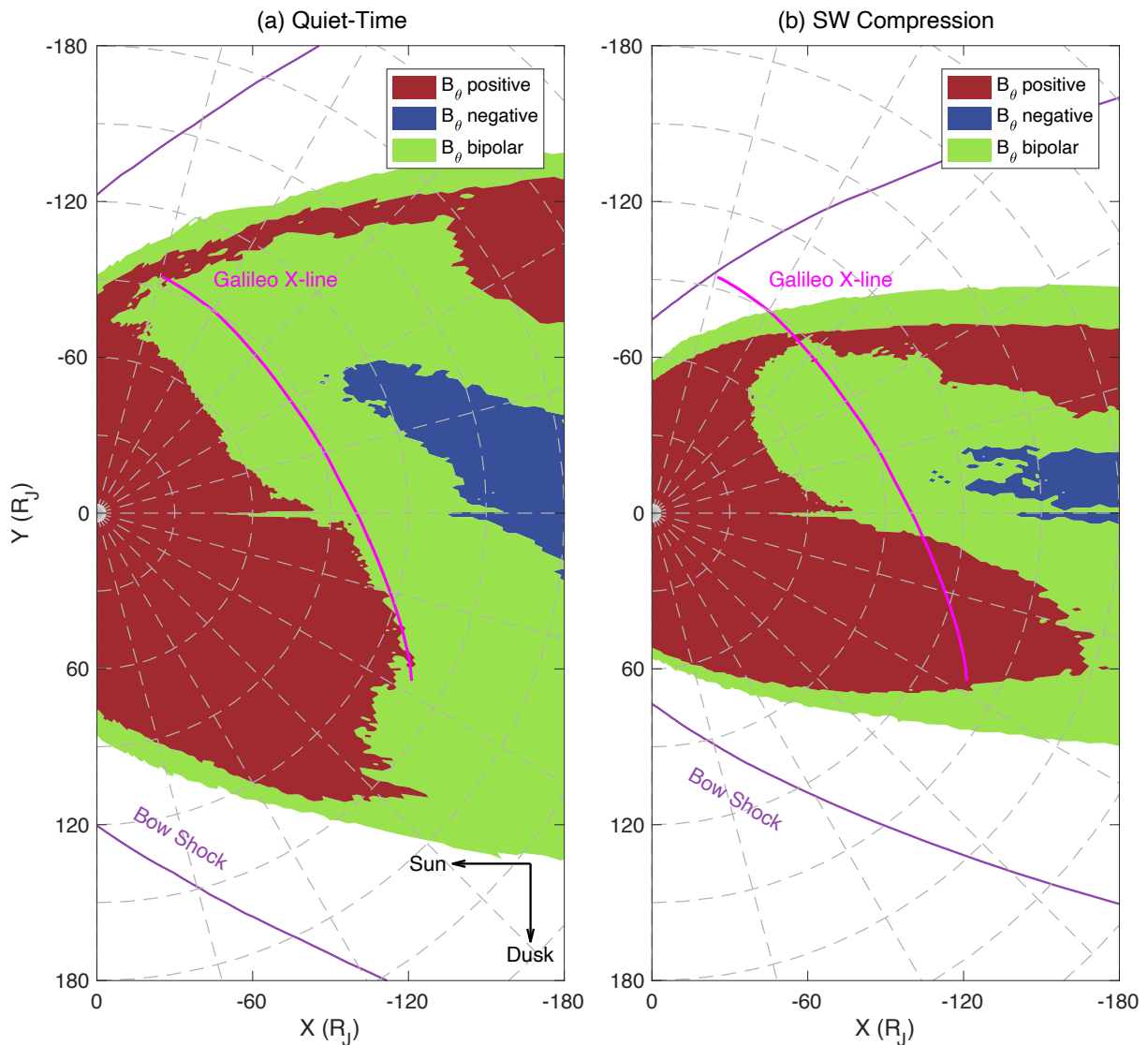
296 dawn-dusk asymmetry is also seen in the Galileo data that has coverage on both dawnside and
 297 duskside for B_z (Vogt et al., 2010) and plasma flow (Woch et al., 2002). As MLT changes from
 298 0:00 to 5:00, the radial position with the maximum occurrence rate decreases from $\sim 120 R_J$ to ~ 80
 299 R_J under SW quiet conditions (Figure 5a), and it decreases from $\sim 110 R_J$ to $\sim 70 R_J$ during SW
 300 compression (Figure 5b). This radial distance-MLT relationship is generally consistent with the
 301 average location of the Galileo-observed X-line (magenta line).

302 In comparison to the quiet-time condition shown in Figure 5a, the enhanced SW ram pressure
 303 results in a higher occurrence of reconnection beyond $60 R_J$ and a slight concentration of
 304 magnetotail reconnection slightly near the midnight sector, as illustrated in Figure 5b. This could
 305 be a result of the impact of SW compression on the equatorial current sheets of giant planets (Smith
 306 et al., 1978; Jackman et al., 2010). Meanwhile, as magnetic reconnection occurs more frequently
 307 at positions closer to Jupiter, which may correspond to greater magnetic energy and a stronger
 308 reconnection energy flux, ultimately resulting in the observed dawn storm auroras during SW
 309 compression periods (Nichols et al., 2007; Nichols et al., 2019; Yao et al., 2022). However, the
 310 changing of the SW ram pressure has a limited impact on magnetotail reconnection during post-
 311 midnight within $60 R_J$, indicating that the generation of Jovian magnetotail reconnection is mostly
 312 driven by the planetary corotation rather than SW effects. In addition, Figure 5 implies that the SW
 313 compression can suppress the reconnection on the duskside (18:00–21:00 MLT), which induces a
 314 stronger dawn-dusk asymmetry of the magnetotail reconnection. This may be attributed to the
 315 smaller volume in the 18:00–21:00 MLT sector in the SW-compressed magnetosphere, which does
 316 not support the centrifugal force to generate sufficient magnetic field line stretching to enable
 317 magnetotail reconnection.

318 To further analyze the distribution of magnetotail reconnection, we statistically analyze the
 319 distribution of the dominant B_θ signature, based on a similar method used in Figures 10–11 of Vogt
 320 et al. (2010). Here, B_θ represents the meridional component of magnetic fields, which is positive
 321 southward at the equatorial plane, i.e., parallel with Jupiter’s dipole magnetic field and opposite to
 322 the B_z definition. Based on the common B_θ directions during a long-term period, each grid point
 323 at the equatorial planes was then assigned one of three B_θ signatures, defined as:

- 324 1) B_θ positive events: B_θ is positive for more than 85% of the event duration, which is the
 325 same definition in Vogt et al. (2010).

- 326 2) B_θ negative events: B_θ is negative for more than 50% of the event duration. We do not
 327 use the same threshold of 85% in Vogt et al. (2010), since few events qualify the 85%
 328 threshold due to the significant dynamic evolution in the magnetotail (as shown in
 329 Movie S1).
- 330 3) B_θ bipolar events: the rest of situations that are neither B_θ positive nor negative events.



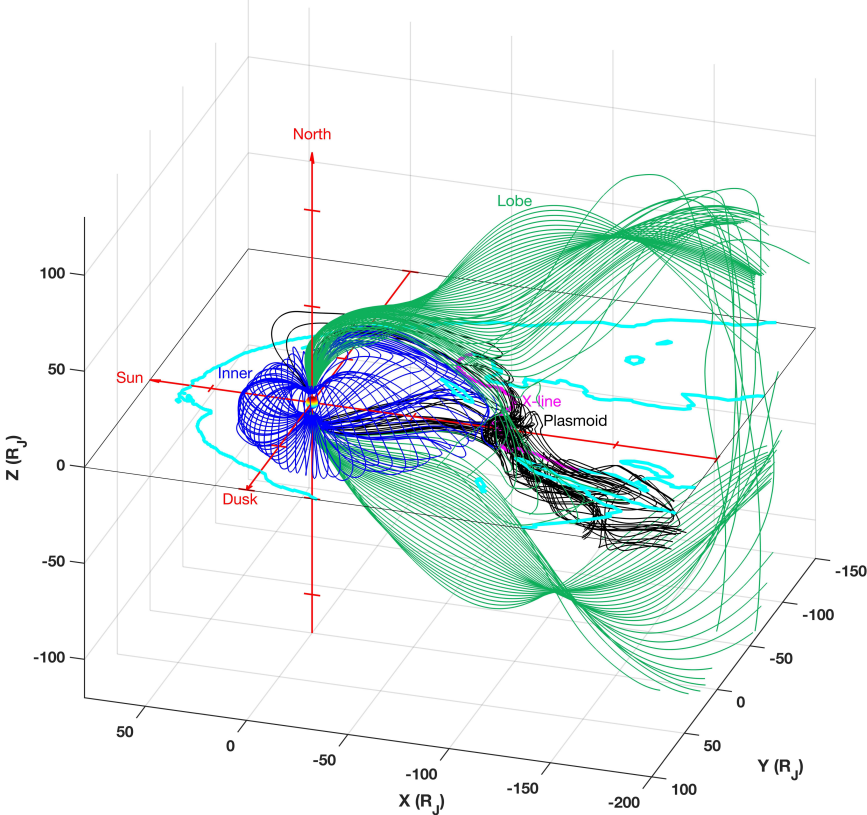
331
 332 **Figure 6.** Distribution of the dominant B_θ signature in the MHD simulation during (a) quiet-time periods between
 333 300:00–345:00 ST and (b) the later phase of SW compression between 360:00–390:00 ST. The colored ranges indicate
 334 the prevalence of different types of events at the calculation grids. Red ranges signify where positive B_θ events are

335 most common (>85%), blue ranges indicate where negative B_{θ} events are most common (>50%), and green ranges
 336 indicate where neither positive nor negative B_{θ} events are dominated. The magenta lines represent the Galileo X-line.
 337 This is an equatorial view with the sun positioned to the left.

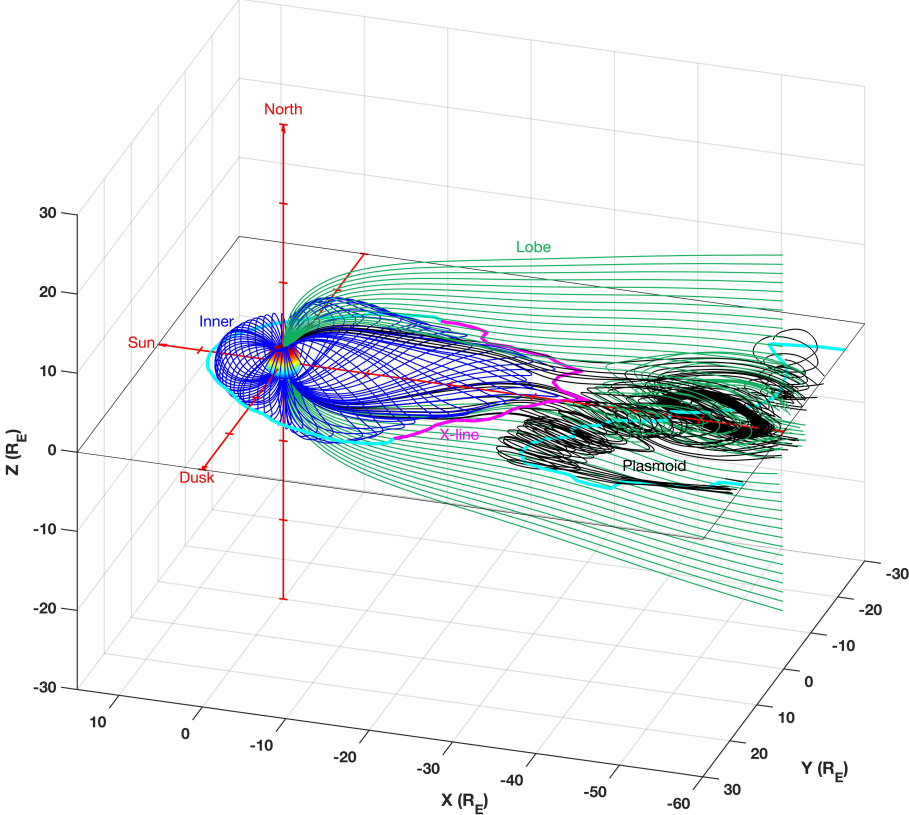
338 Figure 6 illustrates the distribution of the dominant B_{θ} signature and the location of an inferred X-
 339 line during (a) periods of SW quiet time and (b) the later phase of SW compression. Under SW
 340 quiet-time conditions (Figure 6a), the equatorial regions are mostly colored red across most MLTs
 341 and within Jovi-centric $60 R_J$, indicating positive B_{θ} events or inferred inward flows dominate.
 342 Between 21:00 and 5:30 MLT, the inner magnetotail experiences bipolar B_{θ} dominance (green). It
 343 should be noted that the green ranges near the outer boundary of the magnetosphere, which is just
 344 a numerical consequence of the dynamic variation in the size of the magnetosphere. The boundary
 345 between B_{θ} positive and bipolar ranges near the inner magnetotail increases from $\sim 60 R_J$ to ~ 120
 346 R_J with MLT shifting from 5:30 to 21:00, while the boundary between B_{θ} bipolar and negative
 347 ranges near the inner magnetotail increases from $\sim 100 R_J$ to $\sim 180 R_J$ with MLT shifting from 2:00
 348 to 23:30. Moreover, the average locations of the Galileo X-line (magenta line) are located within
 349 the simulated bipolar B_{θ} -dominated ranges, indicating the consistency of the reconnection
 350 positions between the quiet-time MHD simulations and the average satellite observations.

351 When the SW ram pressure is enhanced and the Jovian magnetosphere is significantly compressed
 352 (Figure 6b), the MLT coverage of the bipolar B_{θ} -dominated ranges in the inner magnetotail is
 353 reduced from 21:00–5:30 MLT to 22:30–3:30 MLT. The boundary between B_{θ} positive and bipolar
 354 ranges near the inner magnetotail during SW compression periods is slightly more planetward by
 355 0–10 R_J near and after midnight (after 23:40 MLT), but significantly more tailward by 10–50 R_J
 356 during pre-midnight (before 23:40 MLT) with respect to quiet-time condition (Figure 6a) and the
 357 average Galileo X-line (magenta line in Figure 6). This indicates that the SW compression does not
 358 significantly affect the radial distribution of the average reconnection position near and after
 359 midnight but suppresses reconnection during the pre-midnight. In general, the enhanced ram
 360 pressure can decrease the MLT coverage and induce a larger dawn-dusk asymmetry in the radial
 361 distribution of magnetotail reconnection.

(a) Jupiter



(b) Earth



363 **Figure 7.** Comparison of magnetospheric magnetic field lines associated with magnetotail reconnection at Jupiter and
 364 Earth. Panel (a) depicts the Jovian results obtained from the MHD data with the eastward IMF at 300:00 ST, which is
 365 the same snapshot shown in Figures 3a and 4. Panel (b) shows the terrestrial results from the MHD data with southward
 366 IMF at 23:40 MLT, as used in Zhang et al. (2020). The blue lines indicate the magnetic fields near the inner
 367 magnetosphere, while the green lines represent the lobe magnetic lines through the midnight meridian. The black lines
 368 denote the plasmoid magnetic fields passing through areas outside the locations of the X-line (magenta line).
 369 Additionally, the contours of $B_z = 0$ at the equatorial plane are represented by cyan lines. The colorful spheres
 370 represent the inner boundaries at Jovi-centric $3 R_J$ in the Jovian run and at geocentric 2 Earth radii (R_E) in the terrestrial
 371 run.

372 In Figure 7, the inner magnetic field lines (blue lines) on the planetward side of the X-line are
 373 closed at both planets, but these lines extend from the north to south poles at Jupiter and display
 374 opposite directions at Earth. The plasmoid magnetic field lines (black lines) on the tailward side
 375 of the X-line exhibit turbulent and flux rope structures with multiple twists, indicating that these
 376 complex configurations are a consequence of multiple magnetotail reconnections at different times,
 377 rather than just a single isolated reconnection. These simulations reveal a significant difference
 378 between Jupiter and Earth. Specifically, at Earth, the plasmoid flux rope occurs outside the X-line,
 379 whereas in the Jovian simulation, most of these magnetic field lines revolve around the X-line
 380 itself. This implies the equatorial B_z zero lines, which are used to define the approximate locations
 381 of the X-line in this study and previous observations, may not correspond strictly to the X-line in
 382 the Jovian magnetotail. This discrepancy likely arises from the significant dynamic nature of the
 383 Jovian rotation-driven magnetotail, which lacks the ideal north-south symmetry in the terrestrial
 384 magnetotail. Additionally, different planetary rotation speeds at Jupiter and Earth also cause
 385 significant differences in lobe magnetic field lines near the X-line. Specifically, at Earth, the lobe
 386 magnetic field lines near the X-line through the midnight meridian are open, but in Jupiter, they
 387 exhibit a helical structure and are mostly closed, extending from the polar regions to the distant
 388 tail without east-west components. This unique feature is dominated by Jovian fast rotation, as
 389 demonstrated in the simulation work by Chen et al. (2023) and predicted by the theoretical
 390 frameworks by T. W. Hill (1979) and Isbell et al. (1984).

391 Although most features of the simulated Jovian magnetotail are consistent with satellite
 392 observations and theoretical predictions, other factors, such as dynamic changes in upstream SW
 393 conditions and the presence of hot plasma populations, may also have a significant impact. While
 394 the Jovian magnetosphere remains relatively stable (although still dynamic) during the quiet SW

395 period and the later stages of SW compression (300:00–345:00 and 360:00–390:00 ST), Movie S1
396 displays largely unstable states during the early stages of SW compression at 345:00–360:00 ST.
397 During this period, the magnetosphere experiences rapid compression by the enhanced SW ram
398 pressure, similar to a pressed sponge. Energy and mass are also rapidly released into the far
399 magnetotail. Besides the significantly dynamic response in the Jovian magnetosphere, the field-
400 aligned current and Alfvénic power in the inner magnetosphere or ionosphere also display complex
401 responses (Feng et al., 2022). It is important to note that although this simulation study uses ideal
402 upstream SW conditions, the Jovian magnetospheric responses are still highly dynamic. Therefore,
403 it is expected that Jupiter's magnetosphere is even more complex under changing real SW
404 conditions, though there is not enough upstream SW data available. On the other hand, the MHD
405 simulation does not consider hot plasma populations, resulting in a slightly smaller Jovian
406 magnetosphere (Figure 3) that may influence magnetotail reconnection, especially in the
407 premidnight sector in Figures 5–6. Overall, further investigations are required to fully understand
408 these two effects.

409 **4. Conclusion**

410 In this study, we utilized a three-dimensional global MHD model to simulate Jovian magnetotail
411 reconnection and compared our results with observations from the Galileo and Juno spacecrafts.
412 Our simulations generally reproduce the distribution and occurrence of magnetotail reconnection
413 as observed by both spacecrafts. We discovered that magnetotail reconnection is more frequent in
414 the midnight and post-midnight sectors, but less so in the pre-midnight sector. This is generally
415 consistent with both Galileo and Juno observations and predictions by Delamere and Bagenal
416 (2013). Our simulations indicate that Jovian magnetotail reconnection is dynamic rather than
417 steady-state, with a broad distribution in both MLT and radial distance. The enhanced SW ram
418 pressure can decrease the MLT coverage of magnetotail reconnection by compressing the Jovian
419 magnetosphere. Near the midnight and post-midnight sectors, the occurrence of magnetotail
420 reconnection is enhanced by SW compression beyond $\sim 60 R_J$ but is not significantly impacted by
421 SW compression within $\sim 60 R_J$. On the other hand, SW compression may suppress reconnection
422 in the pre-midnight sector, leading to a stronger dawn-dusk asymmetry in the occurrence and
423 location of magnetotail reconnection.

424 **Acknowledgments**

425 This work is supported by the Excellent Young Scientists Fund (Hong Kong and Macau) of the
 426 National Natural Science Foundation of China (Grant No. 41922060) and RGC General Research
 427 Fund (Grant No. 17308520 and 17315222).

428 **Data Availability Statement**

429 The model outputs used to generate the figures for analysis presented in this paper are being
 430 preserved online (<https://doi.org/10.17605/OSF.IO/5M72X>).

431 **References**

- 432 Ajello, J., Shemansky, D., Pryor, W., Tobiska, K., Hord, C., Stephens, S., Stewart, I., Clarke, J.,
 433 Simmons, K., McClintock, W., Barth, C., Gebben, J., Miller, D., & Sandel, B. (1998).
 434 Galileo Orbiter Ultraviolet Observations of Jupiter Aurora. *Journal of Geophysical*
 435 *Research: Planets*, 103(E9), 20125-20148. <https://doi.org/10.1029/98JE00832>
- 436 Bagenal, F., & Delamere, P. A. (2011). Flow of Mass and Energy in the Magnetospheres of Jupiter
 437 and Saturn. *Journal of Geophysical Research: Space Physics*, 116(A5).
 438 <https://doi.org/10.1029/2010JA016294>
- 439 Biskamp, D. (1996). Magnetic Reconnection in Plasmas. *Astrophysics and Space Science*, 242(1),
 440 165-207. <https://doi.org/10.1007/BF00645113>
- 441 Blanc, M., Kallenbach, R., & Erkaev, N. V. (2005). Solar System Magnetospheres. *Space Science*
 442 *Reviews*, 116(1), 227-298. <https://doi.org/10.1007/s11214-005-1958-y>
- 443 Bonfond, B., Yao, Z., & Grodent, D. (2020). Six Pieces of Evidence against the Corotation
 444 Enforcement Theory to Explain the Main Aurora at Jupiter. *Journal of Geophysical*
 445 *Research: Space Physics*, 125(11), e2020JA028152.
 446 <https://doi.org/10.1029/2020JA028152>
- 447 Brambles, O. J., Lotko, W., Zhang, B., Wiltberger, M., Lyon, J., & Strangeway, R. J. (2011).
 448 Magnetosphere Sawtooth Oscillations Induced by Ionospheric Outflow. *Science*,
 449 332(6034), 1183-1186. <https://doi.org/10.1126/science.1202869>
- 450 Chané, E., Saur, J., & Poedts, S. (2013). Modeling Jupiter's Magnetosphere: Influence of the
 451 Internal Sources. *Journal of Geophysical Research: Space Physics*, 118(5), 2157-2172.
 452 <https://doi.org/10.1002/jgra.50258>
- 453 Connerney, J. E. P., Adriani, A., Allegrini, F., Bagenal, F., Bolton, S. J., Bonfond, B., Cowley, S.
 454 W. H., Gerard, J. C., Gladstone, G. R., Grodent, D., Hospodarsky, G., Jorgensen, J. L.,
 455 Kurth, W. S., Levin, S. M., Mauk, B., McComas, D. J., Mura, A., Paranicas, C., Smith, E.
 456 J., Thorne, R. M., Valek, P., & Waite, J. (2017). Jupiter's Magnetosphere and Aurorae
 457 Observed by the Juno Spacecraft During Its First Polar Orbits. *Science*, 356(6340), 826-
 458 832. <https://doi.org/10.1126/science.aam5928>
- 459 Cowley, S. W. H., Badman, S. V., Imber, S. M., & Milan, S. E. (2008). Comment on "Jupiter: A
 460 Fundamentally Different Magnetospheric Interaction with the Solar Wind" by D. J.
 461 McComas and F. Bagenal. *Geophysical Research Letters*, 35(10).
 462 <https://doi.org/10.1029/2007GL032645>

- 463 Cowley, S. W. H., Bunce, E. J., Stallard, T. S., & Miller, S. (2003). Jupiter's Polar Ionospheric
 464 Flows: Theoretical Interpretation. *Geophysical Research Letters*, 30(5).
 465 <https://doi.org/10.1029/2002GL016030>
- 466 Delamere, P. A., & Bagenal, F. (2010). Solar Wind Interaction with Jupiter's Magnetosphere.
 467 *Journal of Geophysical Research: Space Physics*, 115(A10).
 468 <https://doi.org/10.1029/2010JA015347>
- 469 Delamere, P. A., & Bagenal, F. (2013). Magnetotail Structure of the Giant Magnetospheres:
 470 Implications of the Viscous Interaction with the Solar Wind. *Journal of Geophysical*
 471 *Research: Space Physics*, 118(11), 7045-7053. <https://doi.org/10.1002/2013JA019179>
- 472 Delamere, P. A., Bagenal, F., Paranicas, C., Masters, A., Radioti, A., Bonfond, B., Ray, L., Jia,
 473 X., Nichols, J., & Arridge, C. (2015). Solar Wind and Internally Driven Dynamics:
 474 Influences on Magnetodiscs and Auroral Responses. *Space Science Reviews*, 187(1), 51-
 475 97. <https://doi.org/10.1007/s11214-014-0075-1>
- 476 Feng, E., Zhang, B., Yao, Z., Delamere, P. A., Zheng, Z., Brambles, O. J., Ye, S.-Y., & Sorathia,
 477 K. A. (2022). Dynamic Jovian Magnetosphere Responses to Enhanced Solar Wind Ram
 478 Pressure: Implications for Auroral Activities. *Geophysical Research Letters*, 49(19),
 479 e2022GL099858. <https://doi.org/10.1029/2022GL099858>
- 480 Frank, L. A., Paterson, W. R., & Khurana, K. K. (2002). Observations of Thermal Plasmas in
 481 Jupiter's Magnetotail. *Journal of Geophysical Research: Space Physics*, 107(A1), SIA 1-
 482 1-SIA 1-15. <https://doi.org/10.1029/2001JA000077>
- 483 Gérard, J. C., Mura, A., Bonfond, B., Gladstone, G. R., Adriani, A., Hue, V., Dinelli, B. M.,
 484 Greathouse, T. K., Grodent, D., Altieri, F., Moriconi, M. L., Radioti, A., Connerney, J. E.
 485 P., Bolton, S. J., & Levin, S. M. (2018). Concurrent Ultraviolet and Infrared Observations
 486 of the North Jovian Aurora During Juno's First Perijove. *Icarus*, 312, 145-156.
 487 <https://doi.org/10.1016/j.icarus.2018.04.020>
- 488 Gladstone, G. R., Persyn, S. C., Eterno, J. S., Walther, B. C., Slater, D. C., Davis, M. W., Versteeg,
 489 M. H., Persson, K. B., Young, M. K., Dirks, G. J., Sawka, A. O., Tumlinson, J., Sykes, H.,
 490 Beshears, J., Rhoad, C. L., Cravens, J. P., Winters, G. S., Klar, R. A., Lockhart, W.,
 491 Piepgrass, B. M., Greathouse, T. K., Trantham, B. J., Wilcox, P. M., Jackson, M. W.,
 492 Siegmund, O. H. W., Vallergera, J. V., Raffanti, R., Martin, A., Gérard, J. C., Grodent, D.
 493 C., Bonfond, B., Marquet, B., & Denis, F. (2017). The Ultraviolet Spectrograph on Nasa's
 494 Juno Mission. *Space Science Reviews*, 213(1), 447-473. <https://doi.org/10.1007/s11214-014-0040-z>
- 496 Grodent, D., Bonfond, B., Yao, Z., Gérard, J. C., Radioti, A., Dumont, M., Palmaerts, B., Adriani,
 497 A., Badman, S. V., Bunce, E. J., Clarke, J. T., Connerney, J. E. P., Gladstone, G. R.,
 498 Greathouse, T., Kimura, T., Kurth, W. S., Mauk, B. H., McComas, D. J., Nichols, J. D.,
 499 Orton, G. S., Roth, L., Saur, J., & Valek, P. (2018). Jupiter's Aurora Observed with Hst
 500 During Juno Orbits 3 to 7. *Journal of Geophysical Research: Space Physics*, 123(5), 3299-
 501 3319. <https://doi.org/10.1002/2017JA025046>
- 502 Guo, R. L., Yao, Z. H., Grodent, D., Bonfond, B., Clark, G., Dunn, W. R., Palmaerts, B., Mauk,
 503 B. H., Vogt, M. F., Shi, Q. Q., Wei, Y., Connerney, J. E. P., & Bolton, S. J. (2021). Jupiter's
 504 Double-Arc Aurora as a Signature of Magnetic Reconnection: Simultaneous Observations
 505 from Hst and Juno. *Geophysical Research Letters*, 48(14), e2021GL093964.
 506 <https://doi.org/10.1029/2021GL093964>. 10.1029/2021GL093964

- 507 Hill, M. E., Haggerty, D. K., McNutt Jr, R. L., & Paranicas, C. P. (2009). Energetic Particle
 508 Evidence for Magnetic Filaments in Jupiter's Magnetotail. *Journal of Geophysical*
 509 *Research: Space Physics*, 114(A11). <https://doi.org/10.1029/2009JA014374>
- 510 Hill, T. W. (1979). Inertial Limit on Corotation. *Journal of Geophysical Research: Space Physics*,
 511 84(A11), 6554-6558. <https://doi.org/10.1029/JA084iA11p06554>
- 512 Huscher, E., Bagenal, F., Wilson, R. J., Allegrini, F., Ebert, R. W., Valek, P. W., Szalay, J. R.,
 513 McComas, D. J., Connerney, J. E. P., Bolton, S., & Levin, S. M. (2021). Survey of Juno
 514 Observations in Jupiter's Plasma Disk: Density. *Journal of Geophysical Research: Space*
 515 *Physics*, 126(8), e2021JA029446. <https://doi.org/10.1029/2021JA029446>
- 516 Isbell, J., Dessler, A. J., & Waite Jr, J. H. (1984). Magnetospheric Energization by Interaction
 517 between Planetary Spin and the Solar Wind. *Journal of Geophysical Research: Space*
 518 *Physics*, 89(A12), 10716-10722. <https://doi.org/10.1029/JA089iA12p10716>
- 519 Jackman, C. M., & Arridge, C. S. (2011). Solar Cycle Effects on the Dynamics of Jupiter's and
 520 Saturn's Magnetospheres. *Solar Physics*, 274(1), 481-502. [https://doi.org/10.1007/s11207-](https://doi.org/10.1007/s11207-011-9748-z)
 521 [011-9748-z](https://doi.org/10.1007/s11207-011-9748-z)
- 522 Jackman, C. M., Arridge, C. S., Slavin, J. A., Milan, S. E., Lamy, L., Dougherty, M. K., & Coates,
 523 A. J. (2010). In Situ Observations of the Effect of a Solar Wind Compression on Saturn's
 524 Magnetotail. *Journal of Geophysical Research: Space Physics*, 115(A10).
 525 <https://doi.org/10.1029/2010JA015312>
- 526 Jia, X., Hansen, K. C., Gombosi, T. I., Kivelson, M. G., Tóth, G., DeZeeuw, D. L., & Ridley, A.
 527 J. (2012). Magnetospheric Configuration and Dynamics of Saturn's Magnetosphere: A
 528 Global Mhd Simulation. *Journal of Geophysical Research: Space Physics*, 117(A5).
 529 <https://doi.org/10.1029/2012JA017575>
- 530 Khurana, K. K., Kivelson, M. G., Vasylunas, V. M., Krupp, N., Woch, J., Lagg, A., Mauk, B. H.,
 531 & Kurth, W. S. (2004). The Configuration of Jupiter's Magnetosphere. In (Vol. 1, pp. 593-
 532 616): Cambridge Univ. Press Cambridge, U. K.
- 533 Kronberg, E. A., Woch, J., Krupp, N., Lagg, A., Khurana, K. K., & Glassmeier, K. H. (2005).
 534 Mass Release at Jupiter: Substorm-Like Processes in the Jovian Magnetotail. *Journal of*
 535 *Geophysical Research: Space Physics*, 110(A3). <https://doi.org/10.1029/2004JA010777>
- 536 Kurth, W. S., Sullivan, J. D., Gurnett, D. A., Scarf, F. L., Bridge, H. S., & Sittler Jr, E. C. (1982).
 537 Observations of Jupiter's Distant Magnetotail and Wake. *Journal of Geophysical Research:*
 538 *Space Physics*, 87(A12), 10373-10383. <https://doi.org/10.1029/JA087iA12p10373>
- 539 Lyon, J. G., Fedder, J. A., & Mobarrry, C. M. (2004). The Lyon–Fedder–Mobarrry (Lfm) Global
 540 Mhd Magnetospheric Simulation Code. *Journal of Atmospheric and Solar-Terrestrial*
 541 *Physics*, 66(15), 1333-1350. <https://doi.org/10.1016/j.jastp.2004.03.020>
- 542 Masters, A. (2018). A More Viscous-Like Solar Wind Interaction with All the Giant Planets.
 543 *Geophysical Research Letters*, 45(15), 7320-7329. <https://doi.org/10.1029/2018GL078416>
- 544 Mauk, B. H., Clarke, J. T., Grodent, D., Waite, J. H., Paranicas, C. P., & Williams, D. J. (2002).
 545 Transient Aurora on Jupiter from Injections of Magnetospheric Electrons. *Nature*,
 546 415(6875), 1003-1005. <https://doi.org/10.1038/4151003a>
- 547 McComas, D. J., & Bagenal, F. (2007). Jupiter: A Fundamentally Different Magnetospheric
 548 Interaction with the Solar Wind. *Geophysical Research Letters*, 34(20).
 549 <https://doi.org/10.1029/2007GL031078>
- 550 McComas, D. J., & Bagenal, F. (2008). Reply to Comment by S. W. H. Cowley Et Al. On “Jupiter:
 551 A Fundamentally Different Magnetospheric Interaction with the Solar Wind”. *Geophysical*
 552 *Research Letters*, 35(10). <https://doi.org/10.1029/2008GL034351>

- 553 McNutt, R. L., Haggerty, D. K., Hill, M. E., Krimigis, S. M., Livi, S., Ho, G. C., Gurnee, R. S.,
 554 Mauk, B. H., Mitchell, D. G., Roelof, E. C., McComas, D. J., Bagenal, F., Elliott, H. A.,
 555 Brown, L. E., Kusterer, M., Vandegriff, J., Stern, S. A., Weaver, H. A., Spencer, J. R., &
 556 Moore, J. M. (2007). Energetic Particles in the Jovian Magnetotail. *Science*, *318*(5848),
 557 220-222. <https://doi.org/10.1126/science.1148025>
- 558 Miyoshi, T., & Kusano, K. (2001). A Global Mhd Simulation of the Jovian Magnetosphere
 559 Interacting with/without the Interplanetary Magnetic Field. *Journal of Geophysical*
 560 *Research: Space Physics*, *106*(A6), 10723-10742. <https://doi.org/10.1029/2000JA900153>
- 561 Moriguchi, T., Nakamizo, A., Tanaka, T., Obara, T., & Shimazu, H. (2008). Current Systems in
 562 the Jovian Magnetosphere. *Journal of Geophysical Research: Space Physics*, *113*(A5).
 563 <https://doi.org/10.1029/2007JA012751>
- 564 Nichols, J. D., Bunce, E. J., Clarke, J. T., Cowley, S. W. H., Gérard, J. C., Grodent, D., & Pryor,
 565 W. R. (2007). Response of Jupiter's Uv Auroras to Interplanetary Conditions as Observed
 566 by the Hubble Space Telescope During the Cassini Flyby Campaign. *Journal of*
 567 *Geophysical Research: Space Physics*, *112*(A2). <https://doi.org/10.1029/2006JA012005>
- 568 Nichols, J. D., Kamran, A., & Milan, S. E. (2019). Machine Learning Analysis of Jupiter's Far-
 569 Ultraviolet Auroral Morphology. *Journal of Geophysical Research: Space Physics*,
 570 *124*(11), 8884-8892. <https://doi.org/10.1029/2019JA027120>
- 571 Nishida, A. (1983). Reconnection in the Jovian Magnetosphere. *Geophysical Research Letters*,
 572 *10*(6), 451-454. <https://doi.org/10.1029/GL010i006p00451>
- 573 Ogino, T., Walker, R. J., & Kivelson, M. G. (1998). A Global Magnetohydrodynamic Simulation
 574 of the Jovian Magnetosphere. *Journal of Geophysical Research: Space Physics*, *103*(A1),
 575 225-235. <https://doi.org/10.1029/97JA02247>
- 576 Ouellette, J. E., Brambles, O. J., Lyon, J. G., Lotko, W., & Rogers, B. N. (2013). Properties of
 577 Outflow-Driven Sawtooth Substorms. *Journal of Geophysical Research: Space Physics*,
 578 *118*(6), 3223-3232. <https://doi.org/10.1002/jgra.50309>
- 579 Parker, E. (1979). Cosmical Magnetic Fields. Their Origin and Their Activity. *The International*
 580 *Series of Monographs on Physics*.
- 581 Priest, E., & Forbes, T. (2000). *Magnetic Reconnection: Mhd Theory and Applications*.
 582 Cambridge: Cambridge University Press.
- 583 Russell, C. T., Khurana, K. K., Huddleston, D. E., & Kivelson, M. G. (1998). Localized
 584 Reconnection in the near Jovian Magnetotail. *Science*, *280*(5366), 1061-1064.
 585 <https://doi.org/10.1126/science.280.5366.1061>
- 586 Sarkango, Y., Jia, X., & Toth, G. (2019). Global Mhd Simulations of the Response of Jupiter's
 587 Magnetosphere and Ionosphere to Changes in the Solar Wind and Imf. *Journal of*
 588 *Geophysical Research: Space Physics*, *124*(7), 5317-5341.
 589 <https://doi.org/10.1029/2019JA026787>
- 590 Schok, A. A., Delamere, P. A., Mino, B., Damiano, P. A., Zhang, B., Sciola, A., Sorathia, K.,
 591 Wing, S., Johnson, J. R., Ma, X., Yao, Z., & Brambles, O. (2023). Periodicities and Plasma
 592 Density Structure of Jupiter's Dawnside Magnetosphere. *Journal of Geophysical Research:*
 593 *Planets*, *128*(2), e2022JE007637. <https://doi.org/10.1029/2022JE007637>
- 594 Smith, E. J., Fillius, R. W., & Wolfe, J. H. (1978). Compression of Jupiter's Magnetosphere by the
 595 Solar Wind. *Journal of Geophysical Research: Space Physics*, *83*(A10), 4733-4742.
 596 <https://doi.org/10.1029/JA083iA10p04733>

- 597 Song, P., DeZeeuw, D. L., Gombosi, T. I., Kozyra, J. U., & Powell, K. G. (2001). Global Mhd
598 Simulations for Southward Imf: A Pair of Wings in the Flanks. *Advances in Space*
599 *Research*, 28(12), 1763-1771. [https://doi.org/10.1016/S0273-1177\(01\)00544-0](https://doi.org/10.1016/S0273-1177(01)00544-0)
- 600 Szego, K., Achilleos, N., Arridge, C., Badman, S., Delamere, P., Grodent, D., Kivelson, M. G., &
601 Louarn, P. (2016). *The Magnetodiscs and Aurorae of Giant Planets*: Springer.
- 602 Tanaka, T., Ebihara, Y., Watanabe, M., Fujita, S., & Kataoka, R. (2021). Global Simulation of the
603 Jovian Magnetosphere: Transitional Structure from the Io Plasma Disk to the Plasma Sheet.
604 *Journal of Geophysical Research: Space Physics*, 126(6), e2021JA029232.
605 <https://doi.org/10.1029/2021JA029232>
- 606 Thomas, N., Bagenal, F., Hill, T., Wilson, J., Dowling, T., & McKinnon, W. (2004). Jupiter: The
607 Planet, Satellites and Magnetosphere. *F. Bagenal, T. Dowling, WB McKinnon, Eds*, 561,
608 561-591.
- 609 Vasyliunas, V. M. (1983). Physics of the Jovian Magnetosphere. 11. Plasma Distribution and
610 Flow. *Physics of the Jovian magnetosphere*, 395-453.
- 611 Vogt, M. F., Connerney, J. E. P., DiBraccio, G. A., Wilson, R. J., Thomsen, M. F., Ebert, R. W.,
612 Clark, G. B., Paranicas, C., Kurth, W. S., Allegrini, F., Valek, P. W., & Bolton, S. J. (2020).
613 Magnetotail Reconnection at Jupiter: A Survey of Juno Magnetic Field Observations.
614 *Journal of Geophysical Research: Space Physics*, 125(3), e2019JA027486.
615 <https://doi.org/10.1029/2019JA027486>
- 616 Vogt, M. F., Jackman, C. M., Slavin, J. A., Bunce, E. J., Cowley, S. W. H., Kivelson, M. G., &
617 Khurana, K. K. (2014). Structure and Statistical Properties of Plasmoids in Jupiter's
618 Magnetotail. *Journal of Geophysical Research: Space Physics*, 119(2), 821-843.
619 <https://doi.org/10.1002/2013JA019393>
- 620 Vogt, M. F., Kivelson, M. G., Khurana, K. K., Joy, S. P., & Walker, R. J. (2010). Reconnection
621 and Flows in the Jovian Magnetotail as Inferred from Magnetometer Observations. *Journal*
622 *of Geophysical Research: Space Physics*, 115(A6). <https://doi.org/10.1029/2009JA015098>
- 623 Waite, J. H., Bagenal, F., Seward, F., Na, C., Gladstone, G. R., Cravens, T. E., Hurley, K. C.,
624 Clarke, J. T., Elsner, R., & Stern, S. A. (1994). Rosat Observations of the Jupiter Aurora.
625 *Journal of Geophysical Research: Space Physics*, 99(A8), 14799-14809.
626 <https://doi.org/10.1029/94JA01005>
- 627 Waite, J. H., Gladstone, G. R., Lewis, W. S., Goldstein, R., McComas, D. J., Riley, P., Walker, R.
628 J., Robertson, P., Desai, S., Clarke, J. T., & Young, D. T. (2001). An Auroral Flare at
629 Jupiter. *Nature*, 410(6830), 787-789. <https://doi.org/10.1038/35071018>
- 630 Wang, Y., Guo, X., Tang, B., Li, W., & Wang, C. (2018). Modeling the Jovian Magnetosphere
631 under an Antiparallel Interplanetary Magnetic Field from a Global Mhd Simulation. *Earth*
632 *and Planetary Physics*, 2(4), 303-309. <https://doi.org/10.26464/epp2018028>
- 633 Wang, Y., Yang, J., Guo, X., Wang, C., & Blanc, M. (2023). Simulation of Centrifugally Driven
634 Convection in Jovian Inner Magnetosphere Using the Rice Convection Model. *Journal of*
635 *Geophysical Research: Space Physics*, 128(3), e2022JA031132.
636 <https://doi.org/10.1029/2022JA031132>
- 637 Woch, J., Krupp, N., & Lagg, A. (2002). Particle Bursts in the Jovian Magnetosphere: Evidence
638 for a near-Jupiter Neutral Line. *Geophysical Research Letters*, 29(7), 42-41-42-44.
639 <https://doi.org/10.1029/2001GL014080>
- 640 Yamada, M., Kulsrud, R., & Ji, H. (2010). Magnetic Reconnection. *Reviews of Modern Physics*,
641 82(1), 603-664. <https://doi.org/10.1103/RevModPhys.82.603>

- 642 Yang, J., Wolf, R., Toffoletto, F., Sazykin, S., Wang, W., & Cui, J. (2019). The Inertialized Rice
643 Convection Model. *Journal of Geophysical Research: Space Physics*, 124(12), 10294-
644 10317. <https://doi.org/10.1029/2019JA026811>
- 645 Yao, Z. H., Bonfond, B., Clark, G., Grodent, D., Dunn, W. R., Vogt, M. F., Guo, R. L., Mauk, B.
646 H., Connerney, J. E. P., Levin, S. M., & Bolton, S. J. (2020). Reconnection- and
647 Dipolarization-Driven Auroral Dawn Storms and Injections. *Journal of Geophysical*
648 *Research: Space Physics*, 125(8), e2019JA027663. <https://doi.org/10.1029/2019JA027663>
- 649 Yao, Z. H., Bonfond, B., Grodent, D., Chané, E., Dunn, W. R., Kurth, W. S., Connerney, J. E. P.,
650 Nichols, J. D., Palmaerts, B., Guo, R. L., Hospodarsky, G. B., Mauk, B. H., Kimura, T., &
651 Bolton, S. J. (2022). On the Relation between Auroral Morphologies and Compression
652 Conditions of Jupiter's Magnetopause: Observations from Juno and the Hubble Space
653 Telescope. *Journal of Geophysical Research: Space Physics*, 127(10), e2021JA029894.
654 <https://doi.org/10.1029/2021JA029894>
- 655 Zhang, B., Brambles, O. J., Cassak, P. A., Ouellette, J. E., Wiltberger, M., Lotko, W., & Lyon, J.
656 G. (2017). Transition from Global to Local Control of Dayside Reconnection from
657 Ionospheric-Sourced Mass Loading. *Journal of Geophysical Research: Space Physics*,
658 122(9), 9474-9488. <https://doi.org/10.1002/2016JA023646>
- 659 Zhang, B., Brambles, O. J., Lotko, W., & Lyon, J. G. (2020). Is Nightside Outflow Required to
660 Induce Magnetospheric Sawtooth Oscillations. *Geophysical Research Letters*, 47(6),
661 e2019GL086419. <https://doi.org/10.1029/2019GL086419>
- 662 Zhang, B., Brambles, O. J., Wiltberger, M., Lotko, W., Ouellette, J. E., & Lyon, J. G. (2016). How
663 Does Mass Loading Impact Local Versus Global Control on Dayside Reconnection?
664 *Geophysical Research Letters*, 43(5), 1837-1844. <https://doi.org/10.1002/2016GL068005>
- 665 Zhang, B., Delamere, P. A., Ma, X., Burkholder, B., Wiltberger, M., Lyon, J. G., Merkin, V. G.,
666 & Sorathia, K. A. (2018). Asymmetric Kelvin-Helmholtz Instability at Jupiter's
667 Magnetopause Boundary: Implications for Corotation-Dominated Systems. *Geophysical*
668 *Research Letters*, 45(1), 56-63. <https://doi.org/10.1002/2017gl076315>
- 669 Zhang, B., Delamere, P. A., Yao, Z., Bonfond, B., Lin, D., Sorathia, K. A., Brambles, O. J., Lotko,
670 W., Garretson, J. S., Merkin, V. G., Grodent, D., Dunn, W. R., & Lyon, J. G. (2021). How
671 Jupiter's Unusual Magnetospheric Topology Structures Its Aurora. *Science Advances*,
672 7(15), eabd1204. <https://doi.org/10.1126/sciadv.abd1204>
- 673 Zhang, B., Sorathia, K. A., Lyon, J. G., Merkin, V. G., Garretson, J. S., & Wiltberger, M. (2019).
674 Gamera: A Three-Dimensional Finite-Volume Mhd Solver for Non-Orthogonal
675 Curvilinear Geometries. *The Astrophysical Journal Supplement Series*, 244(1), 20.
676 <https://doi.org/10.3847/1538-4365/ab3a4c>
677